

1 **Direct binding of the flexible C-terminal segment of periaxin to β 4 integrin suggests**
2 **a molecular basis for CMT4F**

3

4 Arne Raasakka¹, Helen Linxweiler¹, Peter J. Brophy², Diane L. Sherman^{2,*}, Petri
5 Kursula^{1,3,*}

6

7 ¹Department of Biomedicine, University of Bergen, Bergen, Norway

8 ²Centre for Discovery Brain Sciences, University of Edinburgh, Edinburgh, United
9 Kingdom

10 ³Faculty of Biochemistry and Molecular Medicine, University of Oulu, Oulu, Finland

11

12 *Corresponding authors: Diane Sherman, Diane.Sherman@ed.ac.uk; Petri Kursula,
13 petri.kursula@uib.no

14

15

16

1 **Abstract**

2

3 The process of myelination in the nervous system requires coordinated formation of
4 both transient and stable supramolecular complexes. Myelin-specific proteins play
5 key roles in these assemblies, which may link membranes to each other or connect
6 the myelinating cell cytoskeleton to the extracellular matrix. The myelin protein
7 periaxin is known to play an important role in linking the Schwann cell cytoskeleton
8 to the basal lamina through membrane receptors, such as the dystroglycan complex.
9 Mutation that truncate periaxin from the C terminus cause demyelinating peripheral
10 neuropathy, Charcot-Marie-Tooth disease type 4F, indicating a function for the
11 periaxin C-terminal region in myelination. We identified the cytoplasmic domain of
12 $\beta 4$ integrin as a specific high-affinity binding partner for periaxin. The C-terminal
13 region of periaxin remains unfolded and flexible when bound to the third fibronectin
14 type III domain of $\beta 4$ integrin. Our data suggest that periaxin is able to link the
15 Schwann cell cytoplasm to the basal lamina through a two-pronged interaction *via*
16 different membrane protein complexes, which bind close to the N and C terminus of
17 this elongated, flexible molecule.

18

1 Introduction

2 Long axonal segments in the vertebrate peripheral nervous system (PNS) are
 3 ensheathed by myelin, which accelerates nerve impulse propagation and which
 4 supports axons both mechanically and trophically (1). A Schwann cell wraps its
 5 plasma membrane, partially excluding its cytosol, several times around a selected
 6 axonal process. This results in compact myelin, which has high lipid and protein
 7 content and is responsible for axonal insulation. Compact myelin is surrounded by a
 8 narrow compartment with higher cytosolic content, non-compact myelin, which acts
 9 as a supportive metabolic compartment to ensure long-term myelin stability (2).
 10 Both myelin compartments contain a specific selection of proteins that have distinct
 11 tasks in ensuring the correct formation and stability of myelin: failure may result in
 12 one of several disease states, including the peripheral inherited neuropathies
 13 Charcot-Marie-Tooth (CMT) disease and Dejerine-Sottas syndrome (DSS). A large
 14 number mutations in different PNS proteins has been linked to these conditions
 15 (3,4). On the other hand, only a handful of CMT mutations have been characterized
 16 at the molecular structural level in order to understand the fine details of disease
 17 mechanisms (5–7).

18 The formation of myelin in the CNS and PNS, as well as its lifelong maintenance,
 19 requires an intricate network of molecular interactions that link the myelin
 20 membrane, the cytoskeleton of the myelinating glial cell, and the extracellular matrix
 21 or the axonal surface together into a large supramolecular complex. A number of
 22 proteins, many of which seem specific for myelinating cells, have been pinpointed as
 23 playing roles in myelination; however, often the molecular details of the relevant
 24 processes and protein-protein interactions remain unknown. Myelin proteins have
 25 been specifically highlighted as a knowledge gap in structural biology in the past (8),
 26 although more structural data from myelin proteins are becoming available.
 27 However, structures of protein-protein complexes of myelin-specific proteins mainly
 28 remain uncharacterized to date.

29 Unlike oligodendrocytic myelin in the CNS, Schwann cells in the PNS are surrounded
 30 by a carbohydrate-rich basal lamina, which is adhered to the outermost (abaxonal)
 31 Schwann cell plasma membrane bilayer *via* dystroglycans and $\alpha 6 \beta 4$ integrin,
 32 contributing to the mechanical stability of myelinated nerves (9–11). Additionally,
 33 non-compact PNS myelin contains tight membrane-apposed structures at the
 34 abaxonal layer. These structures surround cytosolic channels of non-compact myelin,
 35 referred to as Cajal bands, which contain substantial microtubule-based transport as
 36 well as ribosomal activity (12,13). The membrane appositions have tight morphology
 37 and are enriched in periaxin (PRX) – the most abundant PNS non-compact myelin
 38 protein (14). Cajal bands and the membrane appositions are important in regulating
 39 myelin stability. Furthermore, PRX influences the myelin sheath internode distance,
 40 and thus influences nerve conduction velocity (15,16). These structures can be
 41 disturbed in human demyelinating diseases, as well as in corresponding mouse
 42 models (16–19).

43 Two isoforms of PRX are generated through alternative splicing (20). Disease
 44 mutations in PRX often truncate the long C-terminal region of the larger L-PRX
 45 isoform (21). The molecular mechanism of disease in these cases has remained
 46 enigmatic, as the best-characterized protein interactions and functions of L-PRX so

1 far lie very close to the N terminus. These include the PDZ-like domain, which
 2 mediates homo- and heterodimerization of PRX (18,22,23), and the segment after it,
 3 which is known to bind dystrophin-related protein 2 (DRP2) and link PRX to the
 4 dystroglycan complex (18). A conceivable additional mechanism of PRX function and
 5 involvement in disease could involve specific protein interaction sites at the C-
 6 terminal, isoform-specific end of L-PRX.

7 We wanted to identify novel binding partners for the L-PRX C-terminal region. The
 8 third cytoplasmic fibronectin-type III (FNIII) domain of $\beta 4$ integrin ($\beta 4$ -FNIII-3) was
 9 identified as a high-affinity binder, and the complex was characterized using
 10 biophysical and structural biology techniques. The observed direct molecular
 11 interaction is likely to be important for the function of PRX and $\beta 4$ integrin in
 12 developing and mature myelin, and it provides a molecular basis for PRX mutations
 13 in CMT that result in the expression of truncated L-PRX.

14

15

16

17

1 **Materials and methods**

2 **Yeast two-hybrid screening**

3 Yeast two-hybrid screening was performed essentially as previously described (18).
4 Briefly, a random-primed rat sciatic nerve cDNA library in λ ACTII was screened using
5 the C-terminal region of rat L-PRX (residues 681-1383) in the pAS2-1 vector
6 (Clontech) as bait. Three independent clones of β 4 integrin each containing the third
7 FNIII domain were found. To identify the domain of PRX, which interacted with β 4
8 integrin, deletion constructs of PRX were made by PCR and subcloned into pAS2-1.
9 β -galactosidase activity was tested by filter lift assays with one of the β 4 integrin
10 clones (62BpACTII).

11 **GST pulldown**

12 The β 4 integrin FNIII-3 domain (amino acids 1512-1593) cDNA was amplified by PCR
13 and subcloned into pGEXKG. As a control, the adjacent fourth FNIII domain was
14 cloned into the same vector. The recombinant protein was expressed and purified
15 using a Glutathione-Sepharose 4B column as described (18). GST pulldowns were
16 performed by incubation of the GST fusion protein bound to Glutathione-Sepharose
17 with a sciatic nerve lysate, as previously described (18).

18 **Immunoaffinity chromatography**

19 Immunoaffinity pull-downs were performed essentially as described (18). PRX and β 4
20 integrin in the pull-down fractions were identified by Western blot. PRX antibodies
21 have been described (24). Antibodies against β 4 integrin were raised in rabbits using
22 a peptide corresponding to amino acids 1756-1772, to which an N-terminal cysteine
23 was attached for coupling to keyhole limpet hemocyanin (CTEPFLIDGLTLGTQRLE), as
24 described (20).

25 **Immunofluorescence**

26 Mice were perfused intravascularly with 4% paraformaldehyde in 0.1 M sodium
27 phosphate buffer (pH 7.3) and sciatic nerve cryosections were prepared and
28 immunostained as described (25). Antibodies against PRX have been described (26),
29 and the monoclonal antibody against β 4 integrin was a generous gift from Dr. S.J.
30 Kennel, Biology Division, Oak Ridge National Laboratory.

31 **Transfection and coimmunoprecipitation**

32 Full-length cDNA clones encoding rat β 4 integrin and human α 7 integrin were
33 subcloned into the expression vectors pcDNA3.1 and pRC/CMV, respectively, and
34 were generous gifts from Dr M.L. Feltri, Hunter James Kelly Research Institute,
35 University of Buffalo and Dr Arnoud Sonnenberg, Netherlands Cancer Institute. PRX
36 cDNA in the expression vector pCB6 has been described (27). PRX, β 4 integrin, and
37 α 7 integrin were expressed in HEK293 cells. After transfection, the proteins were
38 immunoprecipitated as described (18).

39 **Proteomics**

40 Proteomics analyses were carried out exactly as described (24), comparing the PRX-
41 bound proteomes of PRX^{-/-} mice carrying a transgene for either wild-type PRX
42 (PrxTg/PRX^{-/-}) or PRX with a C-terminal truncation mutation (mouse L-PRX truncated

1 at residue 1016; Δ CPrxTg/PRX^{-/-}) corresponding to human CMT4F R1070X (28,29).
 2 Proteins from mouse nerve lysates were crosslinked followed by
 3 immunoprecipitation with a PRX antibody, and then subjected to mass spectrometry
 4 (MS) analyses. Normalized abundance of β 4 integrin was determined by MS using
 5 Progenesis (Nonlinear Dynamics) as described (24).

6 **Recombinant protein production**

7 Synthetic genes encoding the rat L-PRX C-terminal region (UniProt ID: Q63425,
 8 amino acids 1036 – 1383; PRX-C) and rat β 4-FNIII-3 (UniProt ID: Q64632, amino acids
 9 1512 – 1602) were ordered from DNA2.0 (Newark, CA, USA) in the pJ401 bacterial
 10 expression vector. An additional sequence encoding for an N-terminal hexahistidine
 11 tag, a short linker, and a tobacco etch virus (TEV) protease digestion site
 12 (MHHHHHHSSGVDLGTENLYFQS) were included at the start of the protein-coding
 13 insert.

14 PRX-C was expressed in *E. coli* BL21(DE3) using 0.4 mM IPTG induction for 1.5 h in LB
 15 medium containing 100 μ g/ml ampicillin, at 37 °C. After expression, the cells were
 16 pelleted by centrifugation and sonicated in Ni-NTA washing buffer (40 mM HEPES,
 17 400 mM NaCl, 6 M urea, 20 mM imidazole, 1 mM PMSF, pH 7.5) supplemented with
 18 protease inhibitors (Roche). Purification was performed using Ni-NTA affinity
 19 chromatography and standard procedures. Elution was done with 32 mM HEPES, 320
 20 mM NaCl, 4.8 M urea, 500 mM imidazole, pH 7.5. The eluted fraction was dialyzed at
 21 4 °C with constant stirring against 40 mM HEPES, 400 mM NaCl, 1 mM DTT, pH 7.5,
 22 before addition of recombinant TEV protease for affinity tag removal (30). The
 23 digestion was allowed to proceed overnight while dialyzing, which resulted in
 24 cleaved PRX-C with an additional N-terminal Ser residue. The protein was subjected
 25 to a 2nd Ni-NTA step, in the absence of urea. The unbound and wash fractions were
 26 combined and concentrated, and sequential size exclusion chromatography (SEC) on
 27 a HiLoad Superdex 200 pg 16/600 column (GE Healthcare) was used to separate the
 28 cleaved protein from contaminants and degradation products. Depending on
 29 downstream application, either 20 mM HEPES, 300 mM NaCl, 1% (v/v) glycerol, 0.5
 30 mM TCEP, pH 7.5 (SEC buffer) or 20 mM HEPES, 150 mM NaCl, pH 7.5 (HBS) was
 31 used as running buffer.

32 β 4-FNIII-3 was expressed in *E. coli* BL21(DE3) in LB or TB medium containing 100
 33 μ g/ml ampicillin, with 0.4 mM IPTG induction for 3 h at 37 °C. The cells were
 34 harvested as above and resuspended in 40 mM HEPES, 400 mM NaCl, 20 mM
 35 imidazole, pH 7.5. After lysis by sonication, a Ni-NTA chromatography was carried
 36 out essentially as described above, omitting urea in all buffers. After Ni-NTA, the
 37 eluted protein was directly subjected to SEC using a HiLoad Superdex 75 pg 16/60
 38 column (GE Healthcare) using either HBS or SEC buffer.

39 **Pulldown experiment with purified proteins**

40 Purified recombinant β 4-FNIII-3 and PRX-C were used in pulldown experiments to
 41 confirm the direct interaction. PRX-C with and without the His-tagged β 4-FNIII-3 was
 42 mixed with Ni-NTA agarose for 1 h at +4 °C, in binding buffer (20 mM HEPES, 150
 43 mM NaCl, 20 mM imidazole, pH 7.5). The matrix was collected by centrifugation at
 44 150 g for 5 min at +4 °C. Three washes with binding buffer were carried out, and

1 proteins were eluted with 20 mM HEPES, 150 mM NaCl, 500 mM imidazole, pH 7.5.
2 All fractions were analyzed with SDS-PAGE.

3 In addition, a partially degraded PRX-C sample was employed to identify fragments
4 that do and do not bind β 4-FNIII-3. The pulldown experiment was carried out exactly
5 as above. Bands were excised from the gel and processed for tryptic peptide
6 mapping.

7 **Synchrotron radiation circular dichroism (SRCD) spectroscopy**

8 SRCD data were collected from 0.15 – 0.6 mg ml⁻¹ protein samples in 20 mM Na-
9 phosphate, 150 mM NaF, pH 7.5 on the AU-CD beamline at the ASTRID2 synchrotron
10 (ISA, Aarhus, Denmark). 100- μ m pathlength closed circular cells (Suprasil, Hellma
11 Analytics) were used for the measurements. Spectra were recorded from 170 to 280
12 nm at 20 °C. Temperature scans were performed from 10 to 90 °C in 5 °C intervals,
13 with 5 min incubation per time point prior to spectral acquisition.

14 Buffer spectra were subtracted from the protein samples, and CD units were
15 converted to $\Delta\epsilon$ (M⁻¹ cm⁻¹), using rPRX-C concentration determined using
16 refractometry and/or rFNIII-3 concentration determined using absorbance at 280
17 nm. Deconvolution was performed using DichroWeb (31) with the CDSSTR algorithm
18 (32) and SP175 reference set (33), or using BeStSel (34). Secondary structure
19 prediction was performed using JPred (35).

20 **Small-angle X-ray scattering (SAXS)**

21 Synchrotron SEC-SAXS data for PRX-C, β 4-FNIII-3, and their complex were collected
22 on the B21 beamline at Diamond Light Source (Didcot, UK) using an on-line size
23 exclusion setup: the chromatography was performed using an Agilent 1200-series
24 HPLC system and a Superdex 200 increase 3.2/300GL (GE Healthcare) column with
25 20 mM Tris-HCl, 150 mM NaCl, pH 7.4 as mobile phase at an isocratic flow of 0.04
26 ml/min. 45 μ l injections of 6.5 – 9.8 mg/ml total protein were performed for PRX-C,
27 β 4-FNIII-3, and their equimolar complex (145 μ M each). Scattering was directly
28 recorded from the eluted proteins at 6 s exposure per frame, 591 frames per run.
29 The frames containing a stable R_g within an eluted I_0 peak were selected and
30 combined using ScÅtter (<http://www.bioisis.net/tutorial>). Data were processed and
31 analyzed using the ATSAS package (36). GNOM was used to calculate distance
32 distribution functions (37), and *ab initio* modeling was performed using GASBOR
33 (38). Multiphase modeling of protein complex data was performed using MONSA
34 (39) and ensemble optimization analysis with EOM (40). See Supplementary Table 1
35 for further details.

36 For IDPs, more accurate values of R_g can be obtained from SAXS data using the
37 Debye formalism. Briefly, by plotting $[I(s)]^{-1}$ vs. $s^{2.206}$, in the range $(s R_g)^2 < 3$, one can
38 use much more data than in a regular Guinier plot. Here, a linear fit of the plot is
39 used to obtain $R_g = (a/0.359b)^{0.453}$; a = slope, b = y intercept (41). Theoretical values
40 for R_g and D_{max} for a random chain can be calculated from sequence length as
41 follows: $R_g = R_0 N^v$; $R_0 = 1.98 \text{ \AA}$, N = number of residues, $v = 0.602$ (42) for denatured
42 proteins; $R_0 = 2.54 \text{ \AA}$, $v = 0.522$ (43) for IDPs. Average end-to-end distance can be
43 estimated as $\langle L^2 \rangle = L_0 N$; $L_0 = 81.8 \text{ \AA}$ (42).

44 **Mass spectrometry and covalent crosslinking**

1 The molecular weight of PRX-C and β 4-FNIII-3 was verified by mass spectrometry. In
2 short, the undigested masses were determined using ultra-performance liquid
3 chromatography (UPLC) coupled electrospray ionization (ESI) time-of-flight mass
4 spectrometry in positive ion mode using a Waters Acquity UPLC-coupled Synapt G2
5 mass analyzer with a Z-Spray ESI source.

6 Protein crosslinking was carried out to conjugate surface-exposed carboxylate
7 sidechains with lysines with a zero-length crosslinker. All crosslinking reactions were
8 carried out at 40 μ M final protein concentration in 100 mM bis-tris methane, 150
9 mM NaCl, 4 mM 1-ethyl-3-(3-dimethylaminopropyl)carbodiimide, 20 mM *N*-
10 hydroxysuccinimide, pH 6.5. The activation step was allowed to proceed for 15 min
11 at ambient temperature, followed by quenching the reactions through adding 2-
12 mercaptoethanol to 20 mM. After addition of the second protein in selected
13 reactions, incubation was continued for another 3 h at ambient temperature and
14 stopped by adding ethanolamine to 10 mM. The reactions were analyzed using SDS-
15 PAGE.

16 The crosslinked proteins were identified using matrix-assisted laser
17 desorption/ionization time-of-flight (MALDI-TOF) mass spectrometry. From stained
18 SDS-PAGE gels, gel bands were cut, staining removed by sequential washing with 50
19 mM NH_4HCO_3 in 40% acetonitrile (ACN). Proteins were subjected to in-gel Cys
20 reduction using 20 mM DTT and subsequent alkylation using 40 mM α -
21 iodoacetamide. After this, all proteins were in-gel digested (20 ng of trypsin (Sigma-
22 Aldrich) per gel piece), followed by peptide extraction from gel pieces using 30%
23 ACN/0.1% trifluoroacetic acid (TFA), and transfer to a Bruker anchor plate. 800 μ g/ml
24 α -cyano-4-hydroxy cinnamic acid in 85% ACN/0.1% TFA with 1 mM $\text{NH}_4\text{H}_2\text{PO}_4$ was
25 used as matrix. Peptide mass spectra and MS/MS spectra were measured with a
26 Bruker Ultra flexTreme MALDI-TOF mass spectrometer and compared to theoretical
27 spectra generated using the known protein sequences.

28 **Multi-angle static and quasielastic light scattering**

29 SEC-MALS and quasielastic light scattering (QELS) data were collected to determine
30 the monodispersity, hydrodynamic radius, and molecular weight of PRX-C, β 4-FNIII-
31 3, and their equimolar complex (145 μ M each). The chromatography was performed
32 using an Agilent 1200-series HPLC system and a Superdex 200 increase 3.2/300GL
33 (GE Healthcare) column with 20 mM Tris, 150 mM NaCl, pH 7.4 as mobile phase.
34 Protein samples of 160 – 250 μ g were injected into the column at an isocratic flow of
35 0.04 ml/min, and light scattering was recorded using a Wyatt miniDAWN HELEOS-II
36 instrument with 18 detectors and a QELS module at ambient temperature. The
37 refractive index was measured using a Wyatt Optilab T-rEX refractometer and used
38 as the concentration source. All data were analyzed using the ASTRA software
39 (Wyatt).

40 **Protein crystallography**

41 β 4-FNIII-3 was crystallized using sitting-drop vapor diffusion in drops consisting of
42 150 nl protein solution (12.7 mg/ml in SEC buffer) mixed with 150 nl of reservoir
43 solution. Initially, crystals formed in a wide variety of PEG-based conditions in PACT
44 Premier and JCSG+ (Molecular Dimensions) crystal screens. Optimized crystals used

1 for diffraction data collection were grown at 20 °C in conditions containing 16 – 22%
2 (w/v) PEG 3350 and 180 – 240 mM NH₄NO₃.

3 Prior to diffraction data collection, the crystals were cryoprotected briefly by adding
4 1.5 µl of cryoprotectant solution directly into the sitting drop mix. The
5 cryoprotectant consisted of 75% (v/v) well reservoir and 25% (v/v) PEG 400. After
6 soaking in cryoprotectant, crystals were mounted in loops and snap-frozen in liquid
7 N₂.

8 X-ray diffraction data were collected at 100 K on the P13 beamline, EMBL/DESY,
9 Hamburg, Germany (44) and the ID30A-1 beamline at ESRF (Grenoble, France)
10 (45,46). Data were processed using XDS (47). Phasing was performed with molecular
11 replacement using the human β4-FNIII-3 structure (PDB ID 4wtw) (48) as the search
12 model in Phaser (49). The structure was refined in phenix.refine (50), and model
13 building was done in Coot (51). The low solvent content of 36% (including ordered
14 water) leads to a higher-than-average difference between R_{work} and R_{free} during
15 structure refinement.

16 The structure was validated and analyzed using DSSP (52), MolProbity (53), PyMOL,
17 PDB2PQR (54), APBS (55), and UCSF Chimera (56). The crystal structure was
18 subjected to atomistic molecular dynamics simulations for 550 ns in YASARA (57),
19 essentially as described (58).

20 **Isothermal titration calorimetry (ITC)**

21 PRX-C and β4-FNIII-3 were dialyzed into HBS overnight to ensure matching buffer.
22 The proteins were passed through a 0.22-µm filter, and concentrations were
23 checked. ITC was performed at 25 °C using a Malvern MicroCal iTC200 calorimeter
24 with reference power set to 5 µcal/s. 680 µM β4-FNIII-3 was titrated into 350 µl of
25 68 µM PRX-C under constant stirring. A total of 38 1-µl injections were performed,
26 with a 240-s waiting period between injections. Data were analyzed using Origin. The
27 titration experiment was repeated twice with two separate protein batches and
28 nearly identical values were obtained in each case.

29 **Thermal stability assays**

30 Thermal stability experiments were performed for 0.25 – 2 mg/ml β4-FNIII-3 and a
31 20 µM equimolar complex of PRX-C and β4-FNIII-3 in SEC buffer using a label-free
32 fluorescence-based approach (nanoDSF). The instrument used was a NanoTemper
33 Prometheus NT.48 nanoDSF with a backscattering option to detect aggregation
34 onset. Each 10-µl sample was loaded inside a glass capillary, and a constantly
35 monitored scan from 20 – 95 °C using a 2 °C/min ramp rate was performed.
36 Fluorescence at emission wavelengths 330 nm and 350 nm (F₃₃₀ and F₃₅₀,
37 respectively) was monitored, and a single transition event was observed in the
38 fluorescence ratio (F₃₅₀/F₃₃₀) in all samples. Melting temperature midpoint (T_m)
39 values were extracted from the 1st derivative peak maximum.

40

41

1 Results

2 Identification of the cytoplasmic domain of β 4 integrin as a potential periaxin 3 ligand

4 In order to identify putative protein ligands for the C-terminal segment of L-PRX,
5 which is missing in the presence of the CMT4F R1070X mutation (24,28), we carried
6 out a yeast 2-hybrid screen of a rat sciatic nerve cDNA library with the C-terminal
7 segment, missing upon the R1070X mutation, as bait. As a result, we obtained three
8 separate clones containing the β 4-FNIII-3 domain (Figure 1A). One of these (clone
9 62B) was further used in confirmatory experiments.

10 The interaction was confirmed and the binding site coarsely mapped by using
11 different domains of L-PRX in the screen, with the obtained β 4 integrin construct 62B
12 as bait (Figure 1A). The results indicate that the last ~350 residues, containing the
13 acidic region of L-PRX, are crucial for the interaction in this system. Interestingly,
14 both PRX(996-1165) and PRX(1168-1383) gave negative results, suggesting that the
15 binding site may be located close to the point separating these two constructs, or
16 that the site might be a combination of more than one segment required for high-
17 affinity binding.

18 Evidence for β 4 integrin-PRX interaction in tissues and cells

19 As the next step, GST pulldowns from sciatic nerve lysates were carried out using a
20 GST- β 4-FNIII-3 construct. Western blotting identified L-PRX in the fraction bound to
21 the GST fusion protein, but not GST alone (Figure 1B). DRP2 was also identified in the
22 fraction pulled down by GST- β 4-FNIII-3, while GST- β 4-FNIII-4 was unable to pull
23 down PRX or DRP2 (Supplementary Figure 1). Immunoaffinity pulldowns were
24 further carried out using an anti-PRX antibody, and an analysis of the fractions
25 showed copurification of L-PRX and β 4 integrin (Figure 1C), when SDS - breaking up
26 protein complexes - was not used during extraction.

27 The putative interaction between L-PRX and β 4 integrin was further studied using co-
28 immunoprecipitation from cultured HEK293 cells overexpressing both proteins. After
29 immunoprecipitation with either β 4 integrin or PRX antibodies, both proteins were
30 observed in the eluted fraction, showing they are present in the same complex
31 (Figure 1D).

32 To observe the localization of PRX and β 4 integrin in myelinating glial cells,
33 immunofluorescence staining of mouse sciatic nerves was carried out. The result
34 confirms earlier studies (9,59,60), in that both PRX and β 4 integrin are localized at
35 the outermost membrane layer of myelin (Figure 1E).

36 Changes in the L-PRX interactome in a mouse model of CMT4F

37 Using the mouse model for CMT4F (24), which carries a truncating mutation
38 mimicking human L-PRX with the R1070X mutation, we carried out proteomics
39 experiments to follow the expression level of possible PRX ligand proteins in this
40 model. PRX was immunoprecipitated from mouse nerves after crosslinking, and the
41 bound proteins were analyzed. The levels of DRP2 were decreased in the PRX
42 interactome of these mutant animals (24). In addition, a several-fold drop in the
43 level of β 4 integrin could here be observed in the mutant compared to the wild-type

animals based on data from the same experiment (Figure 1F). The result provides strong evidence for a functional protein complex involving L-PRX and $\beta 4$ integrin in mouse peripheral nerve myelin *in vivo*.

Complex of purified recombinant $\beta 4$ integrin and PRX

The above experiments provided evidence for a direct interaction between L-PRX and $\beta 4$ integrin in myelinating Schwann cells. We conducted a biophysical characterization of the interaction using recombinant PRX-C and $\beta 4$ -FNIII-3.

Pulldown experiments with the purified components confirmed the direct molecular interaction suggested by the data above. His-tagged $\beta 4$ -FNIII-3 pulled down PRX-C (Figure 2A). Pulldown of a partially degraded PRX-C sample showed that essentially all PRX fragments on the SDS-PAGE gel were pulled down by $\beta 4$ -FNIII-3 (Figure 2B); MS analysis indicated that the shortest fragments were missing the very C-terminal regions, while the acidic domain was well-covered in all fragments (data not shown), suggesting that the N-terminal half of the PRX-C construct contained the binding site.

SEC-MALS and QELS experiments verified the interaction *in vitro*, whereby the observed complex mass fit to a 1-to-1 complex, with an increased hydrodynamic radius (R_h) compared to the individual interaction partners alone (Figure 2C, Table 1). R_h of the complex was only slightly higher than that for PRX-C, indicating that the complex remained in an extended overall conformation; this is also reflected in the very small change in SEC elution volume. As $\beta 4$ -FNIII-3 is small and tightly folded, this implicates that the PRX-C segment does not become compact upon complex formation, which would be indicated by a decreased R_h .

A dissociation constant of $1.7 \pm 0.1 \mu\text{M}$ was obtained for the protein-protein complex using ITC, with a binding stoichiometry of ~ 1 (Figure 2D), being in good corroboration with the light scattering data above. Hence, the C-terminal region of L-PRX and $\beta 4$ -FNIII-3 bind each other with a low micromolar affinity, in a complex tight enough to survive *e.g.* separation by SEC. The stoichiometry suggests that the interaction site is either distinct from the repeat sequences in L-PRX, or that maximally one $\beta 4$ integrin molecule can bind to PRX-C even if the binding site would involve the repeats.

Covalent crosslinking and mass spectrometry were used in an attempt to map the binding site in more detail. An additional band containing both proteins was apparent on SDS-PAGE after crosslinking (Figure 2E). MS analysis of tryptic peptides from this band confirmed the presence of both PRX-C and $\beta 4$ -FNIII-3.

Thermal stability of the proteins was studied using label-free differential scanning fluorimetry (nanoDSF), whereby the signal came from the folded $\beta 4$ -FNIII-3 domain. $\beta 4$ -FNIII-3 has the same melting point ($+70^\circ\text{C}$) in the presence and absence of PRX-C (Table 2), suggesting no large structural changes are induced by PRX-C binding.

Structural insights into the protein-protein complex

While PRX-C is predicted to contain segments of β strand, the purified protein is essentially unfolded, as shown by SRCD spectroscopy (Figure 3A, Table 2). The β strand predictions coincide with repeats in the sequence (Figure 3B), and they could

1 be of functional relevance in ligand protein binding and induction of secondary
2 structures in PRX-C.

3 SRCD was used to shed light on possible changes in secondary structure content
4 accompanying complex formation. The spectra clearly show that the overall
5 secondary structure content remains identical in the complex, compared to the two
6 proteins in isolation (Figure 3A). Together with the SAXS data (see below), SRCD
7 shows that upon $\beta 4$ -FNIII-3 binding, the PRX C-terminal segment does not obtain
8 large amounts of folded structure. Heat denaturation experiments by SRCD
9 confirmed the same melting point for $\beta 4$ -FNIII-3 in the presence and absence of PRX-
10 C (Table 2).

11 To aid in structural modelling and understanding the interactions in the complex, we
12 solved the high-resolution crystal structure of the rat $\beta 4$ -FNIII-3 domain (Figure 4,
13 Table 3). The structure is similar to the corresponding human protein (48), consisting
14 of a β sandwich made of 7 β strands. In two of the four monomers in the asymmetric
15 unit, the His tag could be partially seen, being in different conformations (Figure 4).

16 The purified PRX-C was subjected to SAXS experiments to gain more insight into
17 flexibility, molecular dimensions, and conformational ensembles. These experiments
18 indicate that PRX-C behaves much like a random polymer chain and is highly
19 extended (Figure 5, Table 1).

20 While SAXS indicated a highly disordered nature for PRX-C alone, we wanted to see,
21 whether it becomes more ordered in the complex with $\beta 4$ -FNIII-3. The $\beta 4$ -FNIII-3
22 crystal structure was used to model the solution structure of the complex, which
23 cannot be crystallized due to the flexible nature of PRX and the fact that the exact
24 binding site remains unknown. SAXS analysis of the protein complex, based on a SEC-
25 SAXS experiment, shows that PRX-C remains elongated, and extra density
26 corresponding to the size of $\beta 4$ -FNIII-3 appears close to one end of the complex
27 (Figure 5D,E). This is in line with the results from SEC-MALS (see above).

28 The structure of $\beta 4$ -FNIII-3 can be used to predict the binding site for PRX. A surface
29 analysis of the domain indicates an elongated hydrophobic groove lined by β strands
30 4 and 5 (Figure 4,6A), which could accommodate a linear motif, possibly in a β
31 conformation; this could extend the smaller β sheet from 3 to 4 β strands. MD
32 simulations of the structure further show that this region is the most mobile
33 segment of $\beta 4$ -FNIII-3, and the cavity can open even more (Figure 6B-D).
34 Furthermore, although the FNIII-3 and -4 domains of $\beta 4$ integrin are rather
35 homologous, sequence conservation in the possible binding site is very low - in line
36 with the observation that FNIII-4 does not bind to PRX (Supplementary Figure 1).

37

1 Discussion

2 At the cellular level, myelin formation involves a substantial amount of lipid and
3 protein synthesis and their subsequent assembly into a multilayered, tightly packed
4 proteolipid multilayer. The molecular interactions involved in this process can be
5 roughly divided into those involved in the formation of the compact myelin
6 compartment, and into those relevant for non-compact myelin. This division does
7 not imply that a single protein cannot take part in both aspects; for example, MBP
8 functions both in membrane packing and in the regulation of cytoplasmic channels.

9 Both PRX and $\beta 4$ integrin play important roles in peripheral nerve myelination
10 (11,15,25). Recently, it was suggested that PRX may be a ligand for $\beta 4$ integrin (61),
11 and the interaction has been highlighted before (16), but not studied in detail. We
12 set out to confirm this putative direct molecular interaction, and to obtain 3D
13 structural data on the protein-protein complex formed by PRX and $\beta 4$ integrin.

14 L-PRX binds $\beta 4$ integrin directly with high affinity

15 Integrins are involved in myelination by both oligodendrocytes (CNS) and Schwann
16 cells (PNS). In Schwann cells, the two main isoforms of integrin are $\alpha 6\beta 1$ and $\alpha 6\beta 4$.
17 While $\alpha 6\beta 1$ is expressed in the early stages of myelination and is crucial for the radial
18 sorting of axons (62,63), $\alpha 6\beta 4$ is predominant in the late stages and mature myelin
19 (9,59). This indicates a developmental switch during myelination, and suggests $\beta 4$
20 integrin is important for myelin maturation and maintenance. The levels of the
21 Schwann cell laminin receptors integrin $\alpha 6\beta 1$, $\alpha 6\beta 4$ and dystroglycan are all
22 regulated by the transcriptional co-activators Yap and Taz (63). The two basal lamina
23 receptors of mature myelin, $\alpha 6\beta 4$ integrin and dystroglycan, known to be together
24 responsible for myelin stability (11), are according to our results bound to the same
25 scaffold protein, L-PRX, in cytoplasmic membrane appositions of the Schwann cell
26 abaxonal plasma membrane.

27 We have shown here with a collection of methods that L-PRX binds, through its C-
28 terminal region, directly to $\beta 4$ -FNIII-3 with high affinity. Considering the presence of
29 both proteins in a large protein scaffold at the Schwann cell outermost membrane, it
30 is likely that the affinity is even higher, when full-length proteins interact and avidity
31 is increased by *e.g.* protein clustering and oligomerization. PRX could function as a
32 ruler between integrins and dystroglycans on the cell surface; on the other hand,
33 changes in the clustering of these molecules, *e.g.* through changes in the basal
34 lamina, might affect the conformation of PRX as well as its cytosolic interactions.

35 Similarly to the reduction seen here in the PRX interactome of $\beta 4$ integrin in mice
36 with truncated L-PRX, corresponding to human CMT4F mutation R1070X (24), a
37 recent study (61) showed the loss of PRX from the $\beta 4$ integrin interactome in mice
38 with $\beta 4$ integrin deficiency. It was thereby suggested that PRX might link $\beta 4$ integrin
39 functionally to PMP22 (61), but a direct or indirect interaction between PRX and
40 PMP22 remains to be detected.

41 L-PRX is intrinsically disordered

42 The C-terminal segment of L-PRX is highly flexible and intrinsically disordered, as
43 shown by structure predictions, SRCD spectroscopy, and SAXS. The potential of
44 intrinsically disordered regions in mediating specific protein interactions has been

recently highlighted by a number studies (64–66). Such complexes involve usually the recognition of short linear motifs by a folded binding partner. In the current case, PRX-C remains highly flexible even upon $\beta 4$ integrin binding. Considering the ratio R_g/R_h , the complex, having a lower ratio, is likely to be somewhat less flexible than PRX-C alone. Molecular flexibility may be important for the supramolecular organization of the protein scaffold at the outermost layer of PNS myelin, whereby PRX plays a central role.

Intriguingly, many of the myelin-specific proteins have a high degree of intrinsic disorder, as well as specific interactions, which makes myelin an interesting case for studying biomedically relevant intrinsically disordered proteins and their interactions. A well-studied example is the myelin basic protein, which is intrinsically disordered in solution, but partially folds upon membrane binding (67,68). MOBP and the cytoplasmic domain of PO are predicted to be disordered (69), and the latter has been experimentally shown to be intrinsically disordered in solution (70,71). The cytoplasmic domain of the large myelin-associated glycoprotein is an intrinsically disordered protein, but forms a specific heterotetramer upon dynein light chain binding, which is likely to help in dimerization and affect binding to the axonal surface (66).

In addition to the C-terminal segment studied here, most of the L-PRX-specific region is predicted to be intrinsically disordered. Hence, a monomer of L-PRX, assumed to be mainly in random coil conformation, could reach a length of >30 nm (72), which would be nearly doubled in the case of an L-PRX dimer formed through domain swapping at the N-terminal PDZ-like domain (22). PRX may thus be able to act as a molecular ruler and mediate protein interactions across partners distributed widely across the Schwann cell abaxonal membrane. The distance between bound DRP2 and $\beta 4$ integrin can be estimated to be up to ~25-30 nm, depending on the exact binding site and the conformation of L-PRX between the binding sites. The flexibility of L-PRX should allow it to stay bound to both protein complexes, even in the case they rearrange on the membrane.

Insights from structure of the protein complex

The binding site for $\beta 4$ integrin in L-PRX remains unknown, although the mapping in this study has suggested that the acidic region of L-PRX is involved. A sequence alignment of this region (Figure 3B) from different species shows that only a few segments are highly conserved; it is conceivable that these regions have functional relevance and they could form the binding site. Further studies will be required to obtain higher-resolution structural data to fully understand the binding interactions.

Typical modes of target protein binding by FNIII domains include transient opening and domain swapping (73). It is possible that some of the conserved segments in L-PRX are involved in a domain-swapping rearrangement of $\beta 4$ -FNIII-3. Such a mechanism would be compatible with the lack of change in secondary structure content upon complex formation, which we observed in SRCD experiments. High-resolution structural studies should answer many of the currently open questions, which will require the identification of the exact binding site(s).

Considering the structures of both L-PRX and $\beta 4$ integrin, it is possible that additional binding surfaces are present in both proteins. $\beta 4$ integrin has four FNIII domains in

its cytoplasmic domain, and the C-terminal region of L-PRX is large and flexible, containing repetitive sequences. The fourth FNIII domain of $\beta 4$ integrin does not bind to PRX-C (Supplementary Figure 1), however, and it is important to recapitulate that the stoichiometry of the interaction between PRX-C and $\beta 4$ -FNIII-3 was observed here to be 1:1.

Relevance for understanding demyelinating disease

A number of proteins have been characterized as targets for mutations in human hereditary neuropathies, whereby the structure of the myelin sheath is compromised. Detailed knowledge about protein interactions in myelin is required to accurately understand the molecular bases of such diseases. One such protein is PRX, which is expressed as two isoforms, S- and L-PRX. While S-PRX consists of only a dimeric PDZ-like domain and a short tail, L-PRX dimerizes through the N terminus similarly to S-PRX (22), but has in total ~1400 residues. Little is known about the structure and function of these long, repetitive L-PRX-specific segments. Expression of S-PRX may result in PRX heterodimerization (23) and affect the regulation of the PRX-containing protein scaffold, as S-PRX interacts with neither DRP2 nor $\beta 4$ integrin.

Most PRX mutations causing human hereditary neuropathy introduce a premature stop codon into the sequence (74–76). In line with this, patients with such mutations have PRX expressed, but its size is smaller than in normal individuals (29,77). These observations hint at the possibility that an important function of L-PRX during myelin formation and maintenance lies at its C-terminal region. This is intriguing, given our observation that this region of L-PRX is intrinsically disordered. Here, we have shown a tight interaction between this C-terminal region and the third FNIII domain in the $\beta 4$ integrin cytoplasmic domain – in the case of PRX truncations, such an interaction would be abolished. This is expected to cause larger-scale disturbances in the PRX-related protein scaffold reaching to the basal lamina and may translate to defects in myelin maintenance. Interactions with DRP2 are important for PRX function, but for a stable myelin sheath, links between the Schwann cell cytoplasm and the basal lamina through $\beta 4$ integrin may be crucial. L-PRX, hence, mediates a two-pronged interaction from the cytoplasmic side through the Schwann cell plasma membrane to the basal lamina (Figure 7), and might have a role in sequestering different types of laminin receptors.

Loss of O-glycosylation causes similar phenotypic effects as L-PRX truncation in mouse models of CMT4F (78). Several O-glycosylation sites in PRX were identified, and some of them reside in the C-terminal region, which binds $\beta 4$ integrin. It is possible that PTMs, including O-glycosylation, regulate PRX interactions with $\beta 4$ integrin in a dynamic manner.

Integrin $\beta 4$ has been highlighted both as a biomarker for Guillain-Barré syndrome (79–81), an autoimmune demyelinating disease of peripheral nerves, and as a central molecule in the entry of *Mycobacterium leprae* into Schwann cells, via the basal lamina (82). Leprosy is characterized by peripheral nerve damage initiated by mycobacterial infection of the Schwann cells. It is currently not known, how L-PRX binding to $\beta 4$ integrin might modulate this process. Our data provide starting points for such studies in the future.

1 **Concluding remarks**

2 The dimeric, highly elongated, flexible L-PRX is capable of acting as a central protein
3 scaffold within non-compact myelin, linking integrins and dystroglycans together,
4 thus bridging together two major protein complexes linking Schwann cells to the
5 extracellular matrix. This could have high relevance in ensuring the necessary
6 stability of membrane appositions that drive the formation of Cajal bands. The PRX-
7 β 4 integrin complex is likely to be important in both normal myelination, myelin
8 maintenance, as well as the pathophysiology of neurodegenerative disease.
9

1 **Figure legends**

2 **Figure 1. Identification of an interaction between periaxin and β 4 integrin**

3 A. Top: structure of full-length L-PRX and the bait used in a yeast two-hybrid screen
4 using the C terminus of L-PRX (aa 681-1383) fused to the GAL4 DNA-binding domain.
5 Bottom: structure of the intracellular domain of β 4 integrin and one (62B) of the
6 three clones recovered from the screen, all of which included the third FNIII domain
7 of β 4 integrin.

8 B. Identification of the region of PRX, which binds to β 4 integrin. The strength of
9 interaction between the 62B clone and a series of PRX constructs in a yeast two-
10 hybrid β -galactosidase assay was assessed semiquantitatively by the time taken for
11 colonies to turn blue (+++, 30 min; ++, 30–60 min; +, 60–180 min).

12 C. Interaction of β 4-FNIII-3 with PRX *in vitro*. GST or a GST- β 4-FNIII-3 fusion protein
13 were incubated with a sciatic nerve lysate *in vitro* and any bound L-PRX was detected
14 by Western blotting (IB) using a PRX antibody after SDS-PAGE. The input lane
15 confirms the presence of PRX in the lysate. Coomassie blue staining shows that
16 equivalent amounts of GST and the GST fusion proteins were used.

17 D. Immunoaffinity copurification of β 4 integrin and PRX. Detergent extracts of mouse
18 sciatic nerve in the non-ionic detergent Igepal were incubated with beads to which
19 affinity-purified sheep anti-PRX antibodies had been covalently coupled. After
20 extensive washing, bound proteins were eluted and analyzed by SDS-PAGE and
21 Western blotting. The SDS control lane contains proteins that bound to the beads
22 after first solubilizing the nerves in SDS to disrupt protein-protein interactions,
23 followed by dilution of the SDS with Triton X-100.

24 E. Coimmunoprecipitation of β 4 integrin and PRX from transfected HEK293 cells. PRX
25 and β 4 integrin were detected by Western blot (IB) after immunoprecipitation (IP)
26 with β 4 integrin antibodies when β 4 integrin, α 6 integrin, and PRX were
27 coexpressed. Preimmune serum (PI) did not precipitate either protein. Reciprocally,
28 β 4 integrin and PRX were detected by Western blot after immunoprecipitation (IP)
29 with anti-PRX antibodies, when β 4 integrin, α 6 integrin, and PRX were coexpressed.

30 F. Immunohistochemistry. Both PRX (green) and β 4 integrin (red) localize at the
31 abaxonal membrane in mature myelin.

32 G. Quantification of β 4 integrin from the immunoprecipitation of crosslinked sciatic
33 nerves from both the full-length PRX transgenic mouse on a PRX null background
34 (n=3) versus C-terminally truncated PRX transgene on a PRX null background (n=3).

35

36 **Figure 2. Direct molecular interaction assays using purified recombinant proteins.**

37 A. Pulldown with pure recombinant proteins on a Ni-NTA affinity matrix. Top, PRX-C
38 and His-tagged β 4-FNIII-3; middle, PRX-C alone; bottom; partially degraded PRX-C
39 and His-tagged β 4-FNIII-3. Samples: 1, input sample; 2, unbound fraction; 3-5,
40 washes; 6, elution. PRX-C is indicated in red and β 4-FNIII-3 in blue. Sizes of molecular
41 weight markers are indicated on the left (kDa).

- 1 B. Sequence of the PRX-C construct, indicating the presence of acidic and basic
2 repeats. The underlined segment (the acidic domain) can be detected in all the PRX-
3 C bands in the bottom panel of (A).
- 4 C. SEC-MALS analysis shows molecular mass expected for a 1:1 complex. PRX-C, red;
5 β 4-FNIII-3, blue; complex, black.
- 6 D. ITC titration of the complex indicates 1:1 stoichiometry. $\Delta H = 6.2 \pm 0.06$ kcal/mol, ΔS
7 $= 5.8$ cal/mol $^\circ$.
- 8 E. Covalent crosslinking. The complex is only visible, when both proteins have been
9 activated (Lane 1). The magenta arrowhead indicates the 1:1 complex. PRX-C is
10 indicated in red and β 4-FNIII-3 in blue. Samples: 1, both proteins activated; 2, PRX-C
11 activated; 3, PRX-C activated, β 4-FNIII-3 added; 4, no activation; 5, no activation,
12 PRX-C added; 6, no activation, β 4-FNIII-3 added; 7, β 4-FNIII-3 activated; 8, β 4-FNIII-3
13 activated, PRX-C added.

14

15 **Figure 3. L-PRX remains disordered in the complex.**

- 16 A. SRCD spectroscopy. PRX-C, red; β 4-FNIII-3, blue; complex, black; sum of individual
17 protein spectra, magenta.
- 18 B. Secondary structure predictions of the PRX-C acidic region, aligned from selected
19 species.

20

- 21 **Figure 4. Crystal structure of rat β 4-FNIII-3.** Two of the 4 individual chains in the
22 asymmetric unit are shown. The chain is coloured from the N (blue) to the C (red)
23 terminus. The His tag is partially resolved at the N terminus, and takes different
24 conformations in different monomers. Secondary structure elements are labelled.

25

26 **Figure 5. Structure of the complex in solution.**

- 27 A. SAXS scattering curve. PRX-C, red; β 4-FNIII-3, blue; complex, black.
- 28 B. Dimensionless Kratky plot. The black cross indicates the theoretical peak position
29 for a folded, perfectly globular protein.
- 30 C. Distance distribution function.
- 31 D. Multi-phase model from MONSA. PRX-C, pink; β 4-FNIII-3, blue.
- 32 E. Rigid-body fit between a chain-like model of PRX-C (pink) and the integrin crystal
33 structure (blue).
- 34 F. EOM analysis for PRX-C. Dashed lines, theoretical distribution for a random coil;
35 solid lines, the ensemble for PRX-C. Maximum dimension is shown in red and radius
36 of gyration in black. PRX-C is slightly more elongated than a random coil.

37

38 **Figure 6. Possible binding site for L-PRX.**

- 1 A. Surface of the β 4-FNIII-3 crystal structure, coloured by electrostatic potential. The
- 2 predicted binding site is shown by a green dashed line.
- 3 B. MD simulation indicates the possible binding site is flexible (arrow) and may open
- 4 up more.
- 5 C. RMSF during the 550-ns simulation.
- 6 D. Comparison of the start (magenta) and end (yellow/green) points of the
- 7 simulation. The loop at the potential binding site (arrow) is the most mobile region.
- 8 The largest peak in the RMSF plot (panel C) is coloured green in the post-simulation
- 9 structure.

10

11 **Figure 7. Schematic view of the PRX-linked protein scaffold in PNS myelin.**

12

13

1 **Funding**

2 This work was financially supported by the Norwegian Research Council travel grant
3 to PK (SYNKNØYT program), as well as a Wellcome Trust (107008/Z/15/Z) grant to
4 PJB.

5 **Acknowledgements**

6 We gratefully acknowledge the synchrotron radiation facilities and the beamline
7 support at ASTRID2, DLS, ESRF, and EMBL/DESY. We express our gratitude towards
8 the Biocenter Oulu Proteomics and Protein Analysis Core Facility and Dr. Ulrich
9 Bergmann for providing access to mass spectrometric instrumentation, as well as
10 Biophysics, Structural Biology, and Screening (BiSS) facilities at University of Bergen
11 for providing calorimetric equipment and crystallization facilities. We thank Lisa
12 Imrie for performing mass spectrometry and Qiushi Li for assistance. We are grateful
13 to NanoTemper Technologies GmbH and Dr. Teresia Hallström for providing access
14 to nanoDSF instrumentation.

15 **Conflicts of interest**

16 The authors declare that the research was conducted in the absence of any
17 commercial or financial relationships that could be construed as a potential conflict
18 of interest.

19 **Author contributions**

20 PB, DS, and PK conceived of the project. DS and PB carried out and analyzed yeast
21 two-hybrid, immunochemical, and proteomics experiments. AR and HL performed
22 experiments with purified proteins. AR and PK performed analysis of protein
23 structure. AR, DS, and PK drafted the manuscript. All authors contributed to
24 manuscript revision.

25 **Ethical statement**

26 All animal work conformed to United Kingdom legislation (Scientific Procedures) Act
27 1986, and to the University of Edinburgh Ethical Review Committee policy.

28 **Data availability statement**

29 Crystallographic data are available at the Protein Data Bank, under the accession
30 code 6HYF. The raw data supporting the conclusions of this manuscript will be made
31 available by the authors, without undue reservation, to any qualified researcher.

32

Table 1. Characterization of the PRX-C/ β 4-FNIII-3 complex mass and size.

	MS	SEC-MALS			QELS	SEC-SAXS	
	M_r (measured) , Da	M_r (measured), kDa	M_r (theoretical), kDa	% of expected	R_h (nm)	R_g (nm) Guinier/ Debye/ Theoretical denatured, ID P/EOM	D_{max} (nm) GNOM/ Theoretical/EOM
PRX-C	35869	41.00 \pm 0.02	35.87	114	4.79 \pm 0.08	5.68 \pm 0.04/ 6.21/ 6.75, 5.39/6.14	23.0/ 16.9/ 19.6
β 4-FNIII-3	12756	14.30 \pm 0.02	12.76	112	2.15 \pm 0.04	2.11 \pm 0.01/- /-/-	9.8/-/-
complex	-	48.27 \pm 0.04	48.63	99	5.22 \pm 0.08	5.69 \pm 0.06/ 6.11/-/-	25.2/-/-

Table 2. Folding and thermal stability of PRX-C and β 4-FNIII-3.

	SRCD deconvolution*			Secondary structure prediction**			T_m , °C	
	% helix	% strand	% other	% helix	% strand	% other	SRCD	nanoDSF
PRX-C	3 3	38 31	58 66	0	7.7	92.3	-	-
β 4-FNIII-3	1 2	45 50	51 49	0 (0)	37.2 (34.5)	62.8 (65.5)	59.5 \pm 0.6	69.8 \pm 0.1
complex	2 3	39 35	56 61	0	14.9	85.1	58.8 \pm 0.7	70.3 \pm 0.1

* Deconvolved using DichroWeb (values above), or with BeStSel (values below).

** Predicted from primary structures using JPred. Values in brackets were extracted from the crystal structure using DSSP. The complex values were calculated from the JPred predictions, assuming a 1:1 complex.

1 **Table 3. Crystallographic data collection and refinement statistics.**

2 Values in parentheses correspond to the highest-resolution shell.

Data collection statistics	
Beamline	ID30A-1 (ESRF)
Space group	P2 ₁ 2 ₁ 2 ₁
Unit cell <i>a, b, c</i> (Å)	51.22, 52.84, 144.53
Wavelength (Å)	0.966
Resolution (Å)	50-1.60 (1.64-1.60)
Unique reflections	51757 (3746)
Multiplicity	3.3 (3.3)
Completeness (%)	98.3 (98.6)
R _{merge} (%)	6.1 (239.2)
R _{meas} (%)	7.3 (283.9)
<I/σ(I)>	8.8 (0.6)
CC _{1/2} (%)	99.8 (16.6)
Wilson B (Å ²)	39.2
Refinement statistics	
R _{cryst} (%)	19.0
R _{free} (%)	23.9
RMSD bond length (Å)	0.013
RMSD bond angle (°)	1.1
Mean B value (Å ²)	49.7
Ramachandran plot	
Res. in favoured regions (%)	95.9
Outlier residues (%)	0.8
MolProbity score/percentile	2.05 / 44 th
PDB entry	6HYF

3

4

References

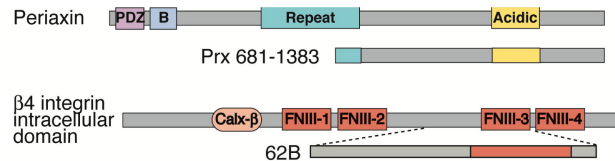
1. Nave KA. Myelination and the trophic support of long axons. *Nat Rev Neurosci* (2010) 11, 275-283.
2. Hartline DK. What is myelin. *Neuron Glia Biol* (2008) 4, 153-163.
3. Boerkoel CF, Takashima H, Garcia CA, Olney RK, Johnson J, Berry K, *et al.* Charcot-Marie-Tooth disease and related neuropathies: mutation distribution and genotype-phenotype correlation. *Ann Neurol* (2002) 51, 190-201.
4. DiVincenzo C, Elzinga CD, Medeiros AC, Karbassi I, Jones JR, Evans MC, *et al.* The allelic spectrum of Charcot-Marie-Tooth disease in over 17,000 individuals with neuropathy. *Mol Genet Genomic Med* (2014) 2, 522-529.
5. Mittendorf KF, Kroncke BM, Meiler J, Sanders CR. The homology model of PMP22 suggests mutations resulting in peripheral neuropathy disrupt transmembrane helix packing. *Biochemistry* (2014) 53, 6139-6141.
6. Ruskamo S, Nieminen T, Kristiansen CK, Vatne GH, Baumann A, Hallin EI, *et al.* Molecular mechanisms of Charcot-Marie-Tooth neuropathy linked to mutations in human myelin protein P2. *Sci Rep* (2017) 7, 6510.
7. Sakakura M, Hadziselimovic A, Wang Z, Schey KL, Sanders CR. Structural basis for the Trembler-J phenotype of Charcot-Marie-Tooth disease. *Structure* (2011) 19, 1160-1169.
8. Xie L, Bourne PE. Functional coverage of the human genome by existing structures, structural genomics targets, and homology models. *PLoS Comput Biol* (2005) 1, e31.
9. Einheber S, Milner TA, Giancotti F, Salzer JL. Axonal regulation of Schwann cell integrin expression suggests a role for alpha 6 beta 4 in myelination. *J Cell Biol* (1993) 123, 1223-1236.
10. Masaki T, Matsumura K, Hirata A, Yamada H, Hase A, Arai K, *et al.* Expression of dystroglycan and the laminin-alpha 2 chain in the rat peripheral nerve during development. *Exp Neurol* (2002) 174, 109-117.
11. Nodari A, Previtali SC, Dati G, Occhi S, Court FA, Colombelli C, *et al.* Alpha6beta4 integrin and dystroglycan cooperate to stabilize the myelin sheath. *J Neurosci* (2008) 28, 6714-6719.
12. Sherman DL, Brophy PJ. Mechanisms of axon ensheathment and myelin growth. *Nat Rev Neurosci* (2005) 6, 683-690.
13. Ushiki T, Ide C. Scanning electron microscopic studies of the myelinated nerve fibres of the mouse sciatic nerve with special reference to the Schwann cell cytoplasmic network external to the myelin sheath. *J Neurocytol* (1987) 16, 737-747.
14. de Monasterio-Schrader P, Jahn O, Tenzer S, Wichert SP, Patzig J, Werner HB. Systematic approaches to central nervous system myelin. *Cell Mol Life Sci* (2012) 69, 2879-2894.
15. Court FA, Sherman DL, Pratt T, Garry EM, Ribchester RR, Cottrell DF, *et al.* Restricted growth of Schwann cells lacking Cajal bands slows conduction in myelinated nerves. *Nature* (2004) 431, 191-195.
16. Wu LM, Williams A, Delaney A, Sherman DL, Brophy PJ. Increasing internodal distance in myelinated nerves accelerates nerve conduction to a flat maximum. *Curr Biol* (2012) 22, 1957-1961.
17. Brennan KM, Bai Y, Pisciotta C, Wang S, Feely SM, Hoegger M, *et al.* Absence of






- 1 Dystrophin Related Protein-2 disrupts Cajal bands in a patient with Charcot-
- 2 Marie-Tooth disease. *Neuromuscul Disord* (2015) 25, 786-793.
- 3 18. Sherman DL, Fabrizi C, Gillespie CS, Brophy PJ. Specific disruption of a schwann
- 4 cell dystrophin-related protein complex in a demyelinating neuropathy. *Neuron*
- 5 (2001) 30, 677-687.
- 6 19. Sherman DL, Wu LM, Grove M, Gillespie CS, Brophy PJ. Drp2 and periaxin form
- 7 Cajal bands with dystroglycan but have distinct roles in Schwann cell growth. *J*
- 8 *Neurosci* (2012) 32, 9419-9428.
- 9 20. Dytrych L, Sherman DL, Gillespie CS, Brophy PJ. Two PDZ domain proteins
- 10 encoded by the murine periaxin gene are the result of alternative intron
- 11 retention and are differentially targeted in Schwann cells. *J Biol Chem* (1998)
- 12 273, 5794-5800.
- 13 21. Takashima H, Boerkoel CF, De Jonghe P, Ceuterick C, Martin JJ, Voit T, *et al.*
- 14 Periaxin mutations cause a broad spectrum of demyelinating neuropathies.
- 15 *Ann Neurol* (2002) 51, 709-715.
- 16 22. Han H, Kursula P. Periaxin and AHNK nucleoprotein 2 form intertwined
- 17 homodimers through domain swapping. *J Biol Chem* (2014) 289, 14121-14131.
- 18 23. Yang Y, Shi Y. L-periaxin interacts with S-periaxin through its PDZ domain.
- 19 *Neurosci Lett* (2015) 609, 23-29.
- 20 24. Sherman DL, Brophy PJ. A murine model of Charcot-Marie-Tooth disease 4F
- 21 reveals a role for the C-terminus of periaxin in the formation and stabilization
- 22 of Cajal bands. *Wellcome Open Res* (2018) 3, 20.
- 23 25. Gillespie CS, Sherman DL, Fleetwood-Walker SM, Cottrell DF, Tait S, Garry EM,
- 24 *et al.* Peripheral demyelination and neuropathic pain behavior in periaxin-
- 25 deficient mice. *Neuron* (2000) 26, 523-531.
- 26 26. Gillespie CS, Sherman DL, Blair GE, Brophy PJ. Periaxin, a novel protein of
- 27 myelinating Schwann cells with a possible role in axonal ensheathment. *Neuron*
- 28 (1994) 12, 497-508.
- 29 27. Sherman DL, Brophy PJ. A tripartite nuclear localization signal in the PDZ-
- 30 domain protein L-periaxin. *J Biol Chem* (2000) 275, 4537-4540.
- 31 28. Otagiri T, Sugai K, Kijima K, Arai H, Sawaishi Y, Shimohata M, *et al.* Periaxin
- 32 mutation in Japanese patients with Charcot-Marie-Tooth disease. *J Hum Genet*
- 33 (2006) 51, 625-628.
- 34 29. Parman Y, Battaloglu E, Baris I, Bilir B, Poyraz M, Bissar-Tadmouri N, *et al.*
- 35 Clinicopathological and genetic study of early-onset demyelinating neuropathy.
- 36 *Brain* (2004) 127, 2540-2550.
- 37 30. van den Berg S, Löfdahl PA, Härd T, Berglund H. Improved solubility of TEV
- 38 protease by directed evolution. *J Biotechnol* (2006) 121, 291-298.
- 39 31. Whitmore L, Wallace BA. DICHROWEB, an online server for protein secondary
- 40 structure analyses from circular dichroism spectroscopic data. *Nucleic Acids*
- 41 *Res* (2004) 32, W668-73.
- 42 32. Johnson WC. Analyzing protein circular dichroism spectra for accurate
- 43 secondary structures. *Proteins* (1999) 35, 307-312.
- 44 33. Lees JG, Miles AJ, Wien F, Wallace BA. A reference database for circular
- 45 dichroism spectroscopy covering fold and secondary structure space.
- 46 *Bioinformatics* (2006) 22, 1955-1962.
- 47 34. Micsonai A, Wien F, Bulayáki É, Kun J, Moussong É, Lee YH, *et al.* BeStSel: a web

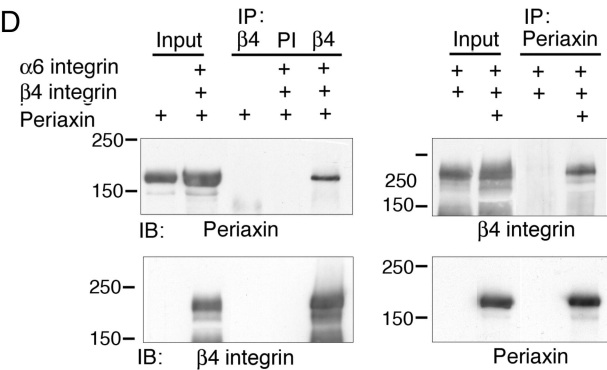
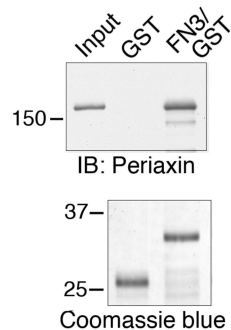
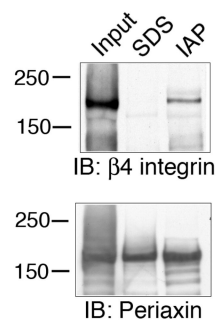
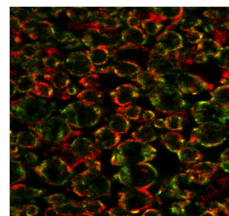
- 1 server for accurate protein secondary structure prediction and fold recognition
- 2 from the circular dichroism spectra. *Nucleic Acids Res* (2018) 46, W315-W322.
- 3 35. Drozdetskiy A, Cole C, Procter J, Barton GJ. JPred4: a protein secondary
- 4 structure prediction server. *Nucleic Acids Res* (2015) 43, W389-94.
- 5 36. Petoukhov MV, Franke D, Shkumatov AV, Tria G, Kikhney AG, Gajda M, *et al.*
- 6 New developments in the ATSAS program package for small-angle scattering
- 7 data analysis. *J Appl Crystallogr* (2012) 45, 342-350.
- 8 37. Svergun DI. Determination of the regularization parameter in indirect-
- 9 transform methods using perceptual criteria. *J Appl Cryst* (1992) 25, 495-503.
- 10 38. Svergun DI, Petoukhov MV, Koch MH. Determination of domain structure of
- 11 proteins from X-ray solution scattering. *Biophys J* (2001) 80, 2946-2953.
- 12 39. Svergun DI. Restoring low resolution structure of biological macromolecules
- 13 from solution scattering using simulated annealing. *Biophys J* (1999) 76, 2879-
- 14 2886.
- 15 40. Bernadó P, Mylonas E, Petoukhov MV, Blackledge M, Svergun DI. Structural
- 16 characterization of flexible proteins using small-angle X-ray scattering. *J Am*
- 17 *Chem Soc* (2007) 129, 5656-5664.
- 18 41. Calmettes P, Durand D, Desmadril M, Minard P, Receveur V, Smith JC. How
- 19 random is a highly denatured protein. *Biophys Chem* (1994) 53, 105-113.
- 20 42. Fitzkee NC, Rose GD. Reassessing random-coil statistics in unfolded proteins.
- 21 *Proc Natl Acad Sci U S A* (2004) 101, 12497-12502.
- 22 43. Bernadó P, Blackledge M. A self-consistent description of the conformational
- 23 behavior of chemically denatured proteins from NMR and small angle
- 24 scattering. *Biophys J* (2009) 97, 2839-2845.
- 25 44. Cianci M, Bourenkov G, Pompidor G, Karpics I, Kallio J, Bento I, *et al.* P13, the
- 26 EMBL macromolecular crystallography beamline at the low-emittance PETRA III
- 27 ring for high- and low-energy phasing with variable beam focusing. *J*
- 28 *Synchrotron Radiat* (2017) 24, 323-332.
- 29 45. Bowler MW, Nurizzo D, Barrett R, Beteva A, Bodin M, Caserotto H, *et al.*
- 30 MASSIF-1: a beamline dedicated to the fully automatic characterization and
- 31 data collection from crystals of biological macromolecules. *J Synchrotron*
- 32 *Radiat* (2015) 22, 1540-1547.
- 33 46. Svensson O, Malbet-Monaco S, Popov A, Nurizzo D, Bowler MW. Fully
- 34 automatic characterization and data collection from crystals of biological
- 35 macromolecules. *Acta Crystallogr D Biol Crystallogr* (2015) 71, 1757-1767.
- 36 47. Kabsch W. XDS. *Acta Crystallogr D Biol Crystallogr* (2010) 66, 125-132.
- 37 48. Alonso-García N, García-Rubio I, Manso JA, Buey RM, Urien H, Sonnenberg A, *et*
- 38 *al.* Combination of X-ray crystallography, SAXS and DEER to obtain the
- 39 structure of the FnIII-3,4 domains of integrin $\alpha 6\beta 4$. *Acta Crystallogr D Biol*
- 40 *Crystallogr* (2015) 71, 969-985.
- 41 49. McCoy AJ, Grosse-Kunstleve RW, Adams PD, Winn MD, Storoni LC, Read RJ.
- 42 Phaser crystallographic software. *J Appl Crystallogr* (2007) 40, 658-674.
- 43 50. Afonine PV, Grosse-Kunstleve RW, Echols N, Headd JJ, Moriarty NW,
- 44 Mustyakimov M, *et al.* Towards automated crystallographic structure
- 45 refinement with phenix.refine. *Acta Crystallogr D Biol Crystallogr* (2012) 68,
- 46 352-367.
- 47 51. Emsley P, Lohkamp B, Scott WG, Cowtan K. Features and development of Coot.

- 1 Acta Cryst D (2010) 66, 486-501.
- 2 52. Kabsch W, Sander C. Dictionary of protein secondary structure: pattern
- 3 recognition of hydrogen-bonded and geometrical features. Biopolymers (1983)
- 4 22, 2577-2637.
- 5 53. Davis IW, Murray LW, Richardson JS, Richardson DC. MOLPROBITY: structure
- 6 validation and all-atom contact analysis for nucleic acids and their complexes.
- 7 Nucleic Acids Res (2004) 32, W615-9.
- 8 54. Dolinsky TJ, Nielsen JE, McCammon JA, Baker NA. PDB2PQR: an automated
- 9 pipeline for the setup of Poisson-Boltzmann electrostatics calculations. Nucleic
- 10 Acids Res (2004) 32, W665-7.
- 11 55. Jurrus E, Engel D, Star K, Monson K, Brandi J, Felberg LE, *et al.* Improvements to
- 12 the APBS biomolecular solvation software suite. Protein Sci (2018) 27, 112-128.
- 13 56. Pettersen EF, Goddard TD, Huang CC, Couch GS, Greenblatt DM, Meng EC, *et*
- 14 *al.* UCSF Chimera--a visualization system for exploratory research and analysis.
- 15 J Comput Chem (2004) 25, 1605-1612.
- 16 57. Krieger E, Vriend G. New ways to boost molecular dynamics simulations. J
- 17 Comput Chem (2015) 36, 996-1007.
- 18 58. Ponna SK, Myllykoski M, Boeckers TM, Kursula P. Structure of an
- 19 unconventional SH3 domain from the postsynaptic density protein Shank3 at
- 20 ultrahigh resolution. Biochem Biophys Res Commun (2017) 490, 806-812.
- 21 59. Feltri ML, Scherer SS, Nemni R, Kamholz J, Vogelbacker H, Scott MO, *et al.* Beta
- 22 4 integrin expression in myelinating Schwann cells is polarized,
- 23 developmentally regulated and axonally dependent. Development (1994) 120,
- 24 1287-1301.
- 25 60. Scherer SS, Xu YT, Bannerman PG, Sherman DL, Brophy PJ. Periaxin expression
- 26 in myelinating Schwann cells: modulation by axon-glial interactions and
- 27 polarized localization during development. Development (1995) 121, 4265-
- 28 4273.
- 29 61. Poitelon Y, Matafora V, Silvestri N, Zambroni D, McGarry C, Serghany N, *et al.* A
- 30 dual role for Integrin $\alpha 6 \beta 4$ in modulating hereditary neuropathy with liability to
- 31 pressure palsies. J Neurochem (2018)
- 32 62. Feltri ML, Graus Porta D, Previtali SC, Nodari A, Migliavacca B, Casseti A, *et al.*
- 33 Conditional disruption of beta 1 integrin in Schwann cells impedes interactions
- 34 with axons. J Cell Biol (2002) 156, 199-209.
- 35 63. Poitelon Y, Lopez-Anido C, Catignas K, Berti C, Palmisano M, Williamson C, *et al.*
- 36 YAP and TAZ control peripheral myelination and the expression of laminin
- 37 receptors in Schwann cells. Nat Neurosci (2016) 19, 879-887.
- 38 64. Barbar E, Nyarko A. Polybivalency and disordered proteins in ordering
- 39 macromolecular assemblies. Semin Cell Dev Biol (2015) 37, 20-25.
- 40 65. Jie J, Löhr F, Barbar E. Interactions of Yeast Dynein with Dynein Light Chain and
- 41 Dynactin: GENERAL IMPLICATIONS FOR INTRINSICALLY DISORDERED DUPLEX
- 42 SCAFFOLDS IN MULTIPROTEIN ASSEMBLIES. J Biol Chem (2015) 290, 23863-
- 43 23874.
- 44 66. Myllykoski M, Eichel MA, Jung RB, Kelm S, Werner HB, Kursula P. High-affinity
- 45 heterotetramer formation between the large myelin-associated glycoprotein
- 46 and the dynein light chain DYNLL1. J Neurochem (2018) 147, 764-783.
- 47 67. Harauz G, Ladizhansky V, Boggs JM. Structural polymorphism and

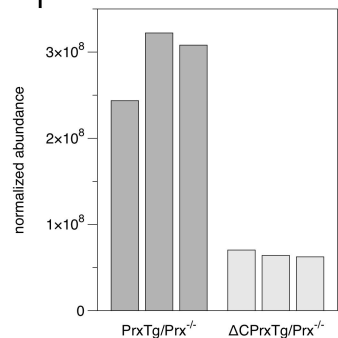
- 1 multifunctionality of myelin basic protein. *Biochemistry* (2009) 48, 8094-8104.
- 2 68. Raasakka A, Ruskamo S, Kowal J, Barker R, Baumann A, Martel A, *et al.*
- 3 Membrane Association Landscape of Myelin Basic Protein Portrays Formation
- 4 of the Myelin Major Dense Line. *Sci Rep* (2017) 7, 4974.
- 5 69. Han H, Myllykoski M, Ruskamo S, Wang C, Kursula P. Myelin-specific proteins: a
- 6 structurally diverse group of membrane-interacting molecules. *Biofactors*
- 7 (2013) 39, 233-241.
- 8 70. Luo X, Sharma D, Inouye H, Lee D, Avila RL, Salmons M, *et al.* Cytoplasmic
- 9 domain of human myelin protein zero likely folded as beta-structure in
- 10 compact myelin. *Biophys J* (2007) 92, 1585-1597.
- 11 71. Raasakka A, Ruskamo S, Kowal J, Han H, Baumann A, Myllykoski M, *et al.*
- 12 Molecular structure and function of myelin protein P0 in membrane stacking.
- 13 *Sci Rep* (2019) in press.
- 14 72. Fitzkee NC, Rose GD. Reassessing random-coil statistics in unfolded proteins.
- 15 *Proc Natl Acad Sci U S A* (2004) 101, 12497-12502.
- 16 73. Ohashi T, Augustus AM, Erickson HP. Transient opening of fibronectin type III
- 17 (FNIII) domains: the interaction of the third FNIII domain of FN with anastellin.
- 18 *Biochemistry* (2009) 48, 4189-4197.
- 19 74. Choi YJ, Hyun YS, Nam SH, Koo H, Hong YB, Chung KW, *et al.* Novel Compound
- 20 Heterozygous Nonsense PRX Mutations in a Korean Dejerine-Sottas
- 21 Neuropathy Family. *J Clin Neurol* (2015) 11, 92-96.
- 22 75. Guilbot A, Williams A, Ravise N, Verny C, Brice A, Sherman DL, *et al.* A mutation
- 23 in periaxin is responsible for CMT4F, an autosomal recessive form of Charcot-
- 24 Marie-Tooth disease. *Hum Mol Genet* (2001) 10, 415-421.
- 25 76. Tokunaga S, Hashiguchi A, Yoshimura A, Maeda K, Suzuki T, Haruki H, *et al.*
- 26 Late-onset Charcot-Marie-Tooth disease 4F caused by periaxin gene mutation.
- 27 *Neurogenetics* (2012) 13, 359-365.
- 28 77. Kabzinska D, Drac H, Sherman DL, Kostera-Pruszczyk A, Brophy PJ, Kochanski A,
- 29 *et al.* Charcot-Marie-Tooth type 4F disease caused by S399fsx410 mutation in
- 30 the PRX gene. *Neurology* (2006) 66, 745-747.
- 31 78. Kim S, Maynard JC, Sasaki Y, Strickland A, Sherman DL, Brophy PJ, *et al.*
- 32 Schwann Cell O-GlcNAc Glycosylation Is Required for Myelin Maintenance and
- 33 Axon Integrity. *J Neurosci* (2016) 36, 9633-9646.
- 34 79. Archelos JJ, Previtali SC, Hartung HP. The role of integrins in immune-mediated
- 35 diseases of the nervous system. *Trends Neurosci* (1999) 22, 30-38.
- 36 80. Previtali SC, Archelos JJ, Hartung HP. Expression of integrins in experimental
- 37 autoimmune neuritis and Guillain-Barré syndrome. *Ann Neurol* (1998) 44, 611-
- 38 621.
- 39 81. Sessa G, Nemni R, Canal N, Marchisio PC. Circulating fragments of myelin-
- 40 associated alpha 6 beta 4 integrin in Guillain-Barré syndrome. *J Neuroimmunol*
- 41 (1997) 80, 115-120.
- 42 82. Rambukkana A, Salzer JL, Yurchenco PD, Tuomanen EI. Neural targeting of
- 43 Mycobacterium leprae mediated by the G domain of the laminin-alpha2 chain.
- 44 *Cell* (1997) 88, 811-821.
- 45
- 46
- 47

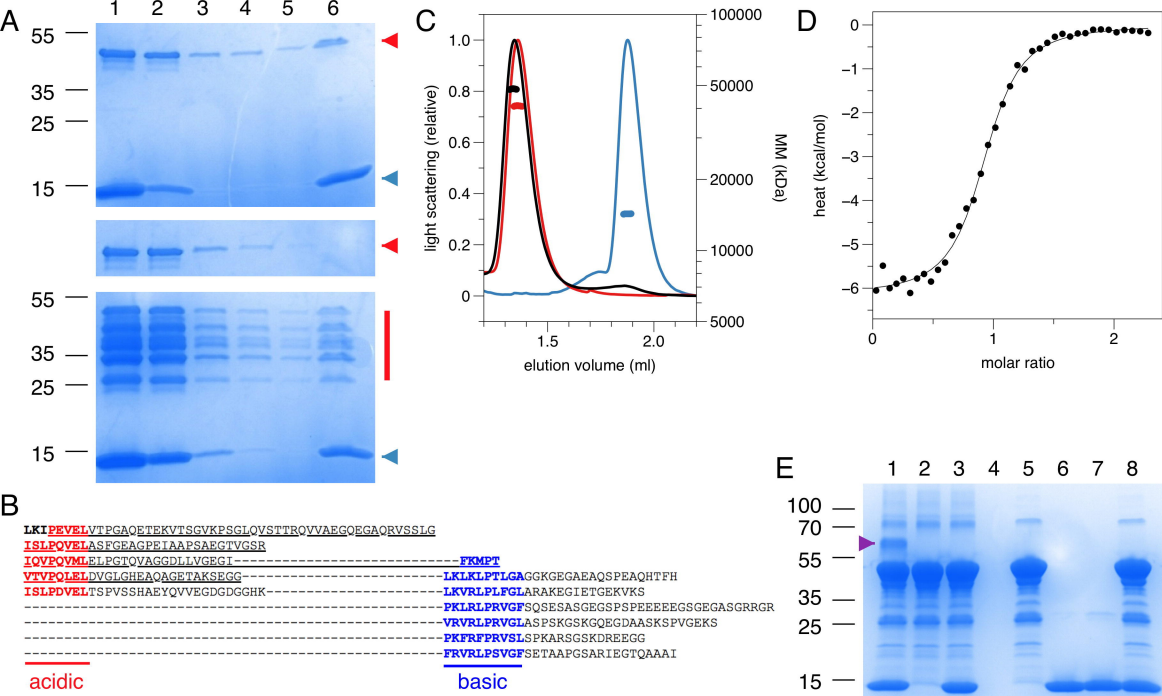
A

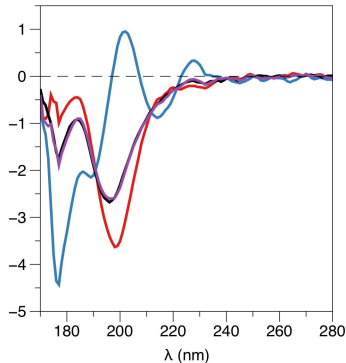
		β gal
Prx 762-1383		+++
Prx 996-1383		+++
Prx 1036-1383		+++
Prx 996-1165		-
Prx 1168-1383		-

D**B****C****E**

PRX
 β 4

F



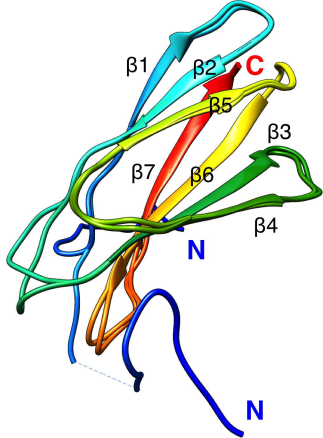
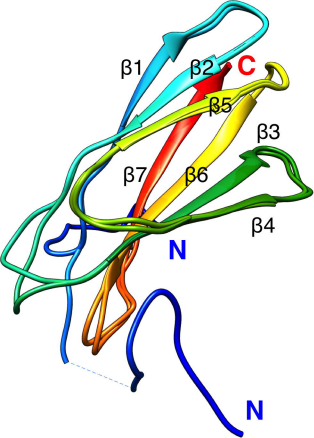
$\Delta\varepsilon \text{ (M}^{-1} \text{ cm}^{-1}\text{)}$ 

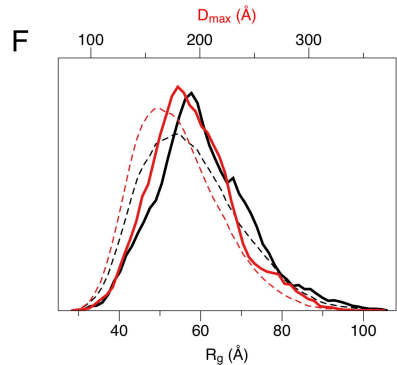
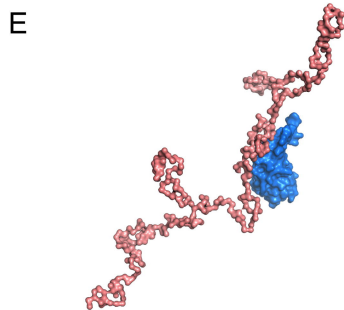
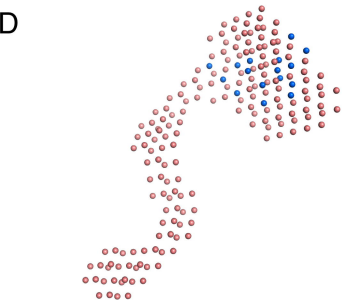
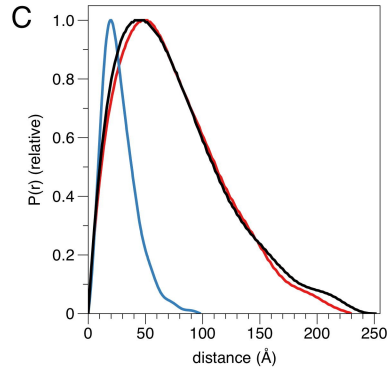
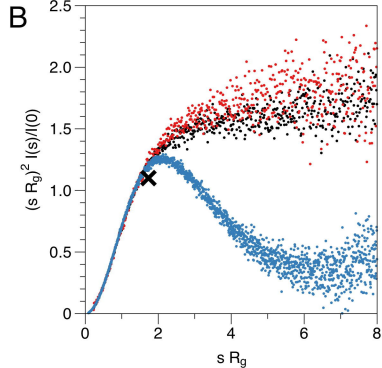
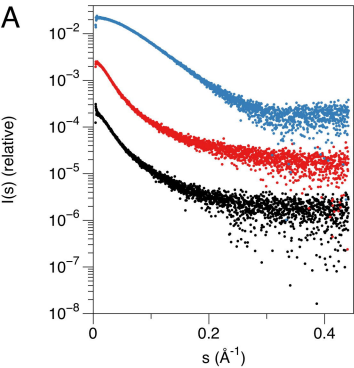
Mus_musculus
Rattus_norvegicus
Jaculus_jaculus
Gorilla_gorilla_gorilla
Homo_sapiens
Elephantulus_edwardii
Heterocephalus_glaber
Equus_caballus
Ceratotherium_simum_simum
Camelus_ferus
Bos_taurus
Capra_hircus
Orcinus_orca
Lipotes_vexillifer
Felis_catus
Ursus_maritimus
Hipposideros_armiger

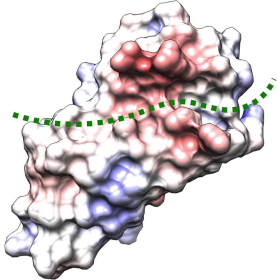
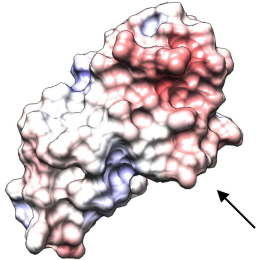
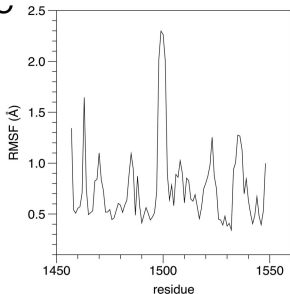
Mus_musculus
Rattus_norvegicus
Jaculus_jaculus
Gorilla_gorilla_gorilla
Homo_sapiens
Elephantulus_edwardii
Heterocephalus_glaber
Equus_caballus
Ceratotherium_simum_simum
Camelus_ferus
Bos_taurus
Capra_hircus
Orcinus_orca
Lipotes_vexillifer
Felis_catus
Ursus_maritimus
Hipposideros_armiger

1050										1060										1070										1080										1090										1100																							
P	A	V	E	L	V	T	P	G	A	Q	E	T	K	V	T	S	G	V	K	P	S	G	L	Q	V	S	T	T	G	V	V	A	E	G	Q	E	S	V	Q	R	V	S	T	L	G	I	S	L	P	Q	V	E	L	A	S	F	G	E	A	G										
P	E	V	E	L	V	T	P	G	A	Q	E	T	K	V	T	S	G	V	K	P	S	G	L	Q	V	S	T	T	R	Q	V	V	A	E	G	Q	E	G	A	Q	R	V	S	T	L	G	I	S	L	P	Q	V	E	L	A	S	F	G	E	A	G									
P	E	V	E	L	V	T	L	G	A	Q	E	G	E	E	A	I	S	V	V	H	P	S	G	L	Q	V	S	V	P	K	Q	A	G	T	E	G	Q	E	G	L	L	R	V	P	T	L	G	I	S	L	P	Q	V	E	L	A	S	F	G	E	A	G								
P	E	V	E	L	V	T	L	G	A	Q	E	E	G	R	A	E	G	A	V	A	V	S	G	M	Q	L	S	G	L	K	V	S	T	A	R	Q	V	T	E	G	H	E	A	G	L	R	M	P	P	L	G	I	S	L	P	Q	V	E	L	T	G	F	G	E	A	G	...	TPR					
P	E	V	E	L	V	T	L	G	A	Q	E	E	G	R	A	E	G	A	V	A	V	S	G	M	Q	L	S	G	L	K	V	S	T	A	R	Q	V	T	E	G	H	D	A	G	L	R	M	P	P	L	G	I	S	L	P	Q	V	E	L	T	G	F	G	E	A	G	...	TPG					
P	E	L	E	L	V	T	L	G	P	E	E	G	R	A	E	G	A	V	A	A	G	R	Q	V	S	M	I	R	K	T	D	S	E	G	Q	E	G	T	L	N	R	P	P	Q	I	S	L	P	Q	V	E	L	T	S	F	G	E	M	G	V	G	A	T	A	G				
P	E	V	E	L	V	T	M	A	A	Q	E	E	S	T	E	G	V	A	A	S	G	V	Q	L	S	A	R	Q	A	T	E	G	R	D	G	V	L	K	M	P	P	L	G	I	S	L	P	Q	V	E	L	T	S	F	G	G	M	G	...	TPG											
P	E	V	E	L	V	T	L	G	A	Q	E	E	G	R	A	E	G	A	V	A	V	S	G	V	R	L	S	G	L	Q	A	S	T	T	R	Q	V	G	T	E	G	Q	D	G	L	R	M	P	P	L	G	I	S	L	P	Q	V	E	L	A	S	F	G	E	A	...	TPG						
P	E	V	E	L	V	T	L	G	A	Q	E	E	G	R	A	E	G	A	V	A	V	S	R	V	R	L	S	G	L	H	V	S	T	T	R	R	V	G	T	E	G	Q	D	A	G	L	R	M	P	P	L	G	I	S	L	P	Q	V	E	L	A	S	F	G	E	A	...	TPG					
P	E	V	E	L	V	T	L	G	A	Q	E	E	G	R	A	E	E	G	V	A	V	S	S	G	R	L	S	G	L	Q	V	S	T	T	R	Q	V	G	T	E	G	Q	D	G	L	R	M	P	P	L	G	I	S	L	P	Q	V	E	L	T	G	F	G	D	V	G	L	G	T	P	G
P	E	V	E	L	V	T	L	G	A	Q	E	E	G	R	V	E	E	E	A	A	G	S	R	G	R	L	A	G	L	Q	V	S	P	A	K	Q	V	G	T	E	A	Q	D	G	L	R	M	P	P	L	G	I	S	L	P	Q	V	E	L	T	G	F	R	E	A	...	TPG						
P	E	V	E	L	V	A	L	G	A	Q	E	E	G	R	V																																																										

111Q						112Q						113Q						114Q						115Q						116Q						117Q					
.PEIVAPS	AEGTAGS	RVQVPQVM	LELPGTQVAGGDL	LVGEGIFKMP	TVTVPQLELDVGL	GHEAQAGEAAKSEGG																																			
.PEIAAPS	AEGTVGS	RIQVPQVM	LELPGTQVAGGDL	LVGEGIFKMP	TVTVPQLELDVGL	GHEAQAGETAKSEGG																																			
.TGTAIPF	ADSTAVS	RVQVPQVT	LELPGTQVVGGDL	LVGEGVFKMP	TVTVPQLELDVGL	NHEAQAGKAADKSG																																			
QAESTVPS	AEGTAGY	RVQVPQVT	LSLPGAQVAGGELL	LVGEGVFKMP	TVTVPQLELDVGL	SREAQAGEAATGEGG																																			
QAESTVPS	AEGTAGY	RVQVPQVT	LSLPGAQVAGGELL	LVGEGVFKMP	TVTVPQLELDVGL	SREAQAGEAATGEGG																																			
QAEGTVPS	AEGTAGS	KVQVPQVT	LALPGAQVAGGELL	LVGEGIFKTPT	TVTVPQLELDVGL	SREAQAGEVAAGEGV																																			
QAEGTAP	TEGTSS	CRVQVPQVS	LSRFGSAAGGELL	LVGEGIFKMP	MVTVPQLELDVGL	SHVQAGEAAAGEGG																																			
QAESAAPP	AEGTAGS	RHVHPQVT	LSLPGAQAAGGELL	LVGEGVFKMP	PAVTVPQLELDVGL	SREAQVGEAATGEGG																																			
QAESAAPP	AEGTAGY	KVQVPQVT	LSLPGVQTASGELL	LVGEGVFKMP	PAVTVPQLELDVGL	SREAQVGEAATGEGG																																			
QAESTAPP	AEGTAGF	KVQVPQVT	LSLPGAQAGAGGELL	LVGEGVFKMP	PAVTVPQLELDVGL	NREAQVGEAATGEGG																																			
QAESSAPP	AEGTAGY	RHVHPQVT	LALPGAQAVGGELL	LVGEGVFKMPS	VTVTVPQLELDVGL	SREVQDGEAATSEGG																																			
QAESSAPL	AEGTAGY	KVHVPQVT	LALPGAQAAGGELL	LVGEGVFKMP	PAVTVPQLELDVGL	SREVQGEAATTSEGG																																			
QAKNAPP	AEGTPGY	RIQVPQVT	LSLPGAQVVGGEPL	ELEGVFKMP	PAVTVPQLELDVGL	SREVQAGEAATGEGA																																			
QAKNAPP	AEGTPDY	RIHVPQVT	LSLPGAQVVGGEPL	VAERVFKMP	PAVTVPQLELDVGL	SREVQVGEAATGEGG																																			
QVKGAAP	AEGTAGY	RVQVPQVT	LSLPGAQVAGGELL	LVGEGVFKMP	PAVTVPQLELDVGL	SREAQVGEAATGEGG																																			
RAKDTAR	VEGTVG	RVQVPQVT	LSLPGAQVAGGELL	LVGEGIFKMP	PAVSVTPQLELDVGL	SREAQSGEAATGEGG																																			
QAESAPP	AEGTAGY	RVQVPQVT	LSLPGAQVASGELL	LVGEGVFKMP	TVTVPQLELDMGL	SREAOLGEAATGEGG																																			





A**B****C****D**